Long-range atmospheric infrasound propagation from subsurface sources

Averbuch, Gil; Assink, Jelle D.; Evers, Läslo G.

DOI
10.1121/10.0000792

Publication date
2020

Document Version
Final published version

Published in
The Journal of the Acoustical Society of America

JASA ARTICLE

Long-range atmospheric infrasound propagation from subsurface sources

Gil Averbuch,[1,a)] Jelle D. Assink,[2,b)] and Läslo G. Evers[2,c)]

[1]*Department of Geoscience and Engineering, Faculty of Civil Engineering and Geosciences, Delft University of Technology, 1 Stevinweg Street, Delft, The Netherlands*

[2]*R&D Department of Seismology and Acoustics, Royal Netherlands Meteorological Institute, P.O. Box 201, 3730 AE De Bilt, The Netherlands*

ABSTRACT:

In seismology and ocean acoustics, the interface with the atmosphere is typically represented as a free surface. Similarly, these interfaces are considered as a rigid surface for infrasound propagation. This implies that seismic or acoustic waves are not transmitted into the atmosphere from subsurface sources, and vice versa. Nevertheless, infrasound generated by subsurface sources has been observed. In this work, seismo-acoustic modeling of infrasound propagation from underwater and underground sources will be presented. The fast field program (FFP) is used to model the seismo-acoustic coupling between the solid earth, the ocean, and the atmosphere under the variation of source and media parameters. The FFP model allows for a detailed analysis of the seismo-acoustic coupling mechanisms in frequency-wavenumber space. A thorough analysis of the coupling mechanisms reveals that evanescent wave coupling and leaky surface waves are the main energy contributors to long-range infrasound propagation. Moreover, it is found that source depth affects the relative amplitude of the tropospheric and stratospheric phases, which allows for source depth estimation in the future. © *2020 Acoustical Society of America*. https://doi.org/10.1121/10.0000792

(Received 16 July 2019; revised 3 February 2020; accepted 6 February 2020; published online 25 February 2020)

[Editor: Philippe Blanc-Benon] Pages: 1264–1274

I. INTRODUCTION

Low-frequency acoustic waves, i.e., infrasound, propagate in the atmosphere in a frequency range between 0.01 to 20 Hz. Infrasonic waves in the atmosphere may originate from sources in all geophysical media, such as the solid Earth, the oceans, and the atmosphere. Examples of infrasound sources include underground explosions, earthquakes, and volcanoes.[1] Due to the high impedance contrast, the Earth-atmosphere and ocean-atmosphere interfaces are typically treated as a free surface.[2] Wave physics predicts transmission on the order of the impedance contrast, which is less than one-hundredth of a percent. Moreover, the coupled waves are confined within a narrow cone around the vertical axis, which is defined by the critical angle. Waves propagating at such steep angles do not get trapped in atmospheric waveguides and do not travel over long distances. Therefore, wavefields that are generated in the Earth and oceans are not expected to be detected in the atmosphere. Nevertheless, observations of infrasound signals from underwater and underground sources contradict this traditional assumption. Such events are known as seismo-acoustic events.

A seismo-acoustic event is an event for which the seismic wavefield in Earth and the acoustic wavefield in the oceans and/or the atmosphere are coupled and have been generated by the same source. Benioff *et al.*[3] were the first to detect acoustic arrivals caused by an earthquake of unknown magnitude at a distance of 265 km. Following that, infrasonic observations of the 1964 M_w 9 Alaska earthquake have been studied in detail and have been associated with epicentral infrasound[4–6] as well as secondary radiation from mountain ranges.[7] It was proposed that the infrasound was locally coupled to the atmosphere through the passage of Rayleigh waves.

Vice versa, atmospheric sources can also lead to seismo-acoustics events, as the infrasound waves can readily couple to seismic waves. Ben-Menahem and Vered[8] investigated the generation of seismic waves from atmospheric nuclear explosions. In August 1989, the return of the Columbia space shuttle generated an atmospheric shock wave that coupled to seismic P waves,[9] and in February 2013, the shock wave from the breakup of the Chelyabinsk meteor excited Rayleigh waves that were recorded at distances up to 4000 km.[10]

Since the 1960s, various other studies have focused on the analysis of infrasound associated with earthquakes. Usually, such signals are assigned to the interaction of seismic body waves and surface waves with topographic features at the epicenteral region.[11–14] However, efficient coupling also occurs remotely from the source epicenter in sedimentary basins and mountainous areas.[15–17] Such coupling may be observed when propagation paths are efficient from such regions to the observing infrasound array.[17] Thus, different infrasound arrays may observe different regions of

[a)]Also at: R&D Department of Seismology and Acoustics, Royal Netherlands Meteorological Institute, De Bilt, The Netherlands. Electronic mail: g.averbuch@tudelft.nl, ORCID: 0000-0002-0403-9354.

[b)]ORCID: 0000-0002-4990-6845.

[c)]Also at: Department of Geoscience and Engineering, Faculty of Civil Engineering and Geosciences, Delft University of Technology, Delft, The Netherlands, ORCID: 0000-0003-2825-6211.

https://doi.org/10.1121/10.0000792

efficient coupling.[15] In addition, evidence for seismo-acoustic events can also be found in the ionosphere; measurements of perturbations in the ionospheric total electron content have been linked to air-coupled surface waves following large earthquakes.[18]

Seismo-acoustic events also exist in an Earth-ocean-atmosphere system. In 2004, a M_w 8.1 earthquake near Macquarie Ridge generated infrasound waves that were detected at a distance of 1300 km. The observations could be qualitatively explained by the coupling of seismic to hydroacoustic waves and then to infrasound waves in the atmosphere.[19] The 2017 North Korean nuclear test also led to a seismo-acoustic event that included complex Earth-atmosphere and Earth-ocean-atmosphere coupling, both above the epicenter as well as from regions further away from the test site.[20]

Analytic studies attribute sound transmission through the ocean-atmosphere and Earth-atmosphere interfaces to two primary mechanisms that are frequency and wavenumber dependent. These mechanisms consist of air-coupled surface waves and enhanced transmission of inhomogeneous body waves. However, the effect of these mechanisms has not been investigated regarding long-range sound propagation. The goal of this work is to numerically study the effect of these mechanisms on long-range infrasound propagation from underwater and underground sources.

The paper is organized as follows. Section II provides an overview of the different coupling mechanisms. For convenience, the coupling mechanisms are discussed regarding Earth-atmosphere (solid-fluid) and ocean-atmosphere (fluid-fluid) systems. Nevertheless, the theory holds for any arbitrary solid-fluid or fluid-fluid system. The theory of retrieving the seismo-acoustic wavefield in a horizontally layered medium is explained in Sec. II. Numerical investigation of long-range infrasound propagation from subsurface sources is presented in Sec. IV and the conclusions are drawn in Sec. V.

II. COUPLING MECHANISM

Coupling of seismo-acoustic energy into the atmosphere happens in both ocean-atmosphere and Earth-atmosphere systems. Efficient coupling is attributed to three types of waves that are associated with different parts of the wavefield spectrum. These waves can be distinguished by their horizontal phase velocity, which is known as trace velocity. The first type is homogeneous P and S waves. These waves consist of relatively high trace velocities, that once in the atmosphere, propagate almost vertically. Consequently, in a horizontally layered system, these waves cannot get trapped in the atmospheric waveguides, therefore having the smallest contribution to long-range infrasound propagation.

The second type is inhomogeneous body waves, which are also known as evanescent waves. These waves have trace velocities that are lower than the medium velocity and therefore have an imaginary vertical wavenumber components, resulting in an exponential decay in amplitude. Let us define k as the source's medium wavenumber, and z_s as the source depth. Theory predicts that for a non-dimensional source depth, kz_s, smaller than 1, the interface (ocean-atmosphere or Earth-atmosphere) becomes transparent to the evanescent spectrum; allowing all the evanescent energy to radiate into the atmosphere. Moreover, the emitted pressure field into the air can be up to three orders of magnitude greater than for kz_s larger than 1.[21–23] The contribution of this mechanism is twofold; besides emitting most of their energy into the air, evanescent waves in the earth or ocean consist of a large horizontal wavenumber component. Therefore, once in the atmosphere, these waves become oscillatory in the air, get trapped in the atmospheric waveguides, and propagate over hundreds and thousands of kilometers.

The third type is surface waves. Surface waves propagate along the free-surface of an elastic half-space, and they are a linear combination of elastic inhomogeneous body waves.[24] In a coupled elastic-acoustic system, combining their solutions with a propagating or evanescent acoustic waves in the acoustic layer give rise to leaky Rayleigh (evanescent-propagating) or Stoneley (evanescent-evanescent) waves, respectively.[25–27] In contrast, Love waves would not contribute to coupled seismo-acoustic waves due to their horizontal polarization. The existence of such waves is determined by the elastic and acoustic properties, i.e., densities and Lamé parameters.[28,29]

Such waves exist in an Earth-atmosphere system. Ewing and Ben-Menahem studied the generation of Rayleigh waves from atmospheric explosions.[30,31] Moreover, Ewing *et al.*[30] have shown that some of the Rayleigh wave energy can radiated back into the atmosphere. Thus, surface waves generated from an underground source can also radiate acoustic waves into the atmosphere. While this mechanism is less sensitive to the source depth, the vertical angle of propagation in the atmosphere depends on the surface wave velocity v_{surface} and the atmospheric speed of sound c_{air}. For $v_{\text{surface}} \gg c_{\text{air}}$, the radiated wave will propagate vertically upwards. The vertical angle decreases as v_{surface} approaches the atmospheric sound speed, to the limit where the vertical angle is zero. Beyond this angle, for which $v_{\text{surface}} < c_{\text{air}}$, the acoustic wave propagates horizontally and decays vertically; this corresponds to a Stoneley wave.

The transparency of the interface also depends on the source type (monopole, dipole, etc.) and the attenuation coefficients in the elastic medium.[32] Attenuation changes the behavior of transparency as a function of kz_s, as well as the relative contribution of the different seismic waves to the total emitted energy. Variations in these parameters can result in more than a 20 dB difference in the emitted acoustic amplitudes.[32]

III. RETRIEVING THE SEISMO-ACOUSTIC WAVEFIELD

Modeling elastic and acoustic wavefields requires solving the elastic wave equation and the linearized fluid dynamics equations. Both sets of equations are based on the

conservation of mass, momentum equation, and an equation of state. The elastic equation of motion for the displacement $\boldsymbol{u}$ can be written as[33]

$$\rho_0 \frac{\partial^2 \boldsymbol{u}}{\partial t^2} - \nabla \cdot \boldsymbol{\sigma} = 0, \tag{1}$$

where $\boldsymbol{\sigma}$ is the stress tensor, and ρ_0 is the density. The elastic wave equation can be obtained by combining Eq. (1) with the complemented Hooke's law for isotropic media

$$\boldsymbol{\sigma} = \lambda tr(\boldsymbol{\epsilon}) I + 2\mu \boldsymbol{\epsilon}; \quad \boldsymbol{\epsilon} = \frac{1}{2}\left(\nabla \boldsymbol{u} + (\nabla \boldsymbol{u})^T\right), \tag{2}$$

where I is an identity matrix, λ and μ are the Lamé parameters, and $\boldsymbol{\epsilon}$ is the strain. The normal stress relates to the pressure in a fluid media according to $\sigma_{zz} = -p$.

For a moving medium, combining the momentum equation, conservation of mass, and the equation of state yields the infrasound wave equation. Assuming a horizontally layered lossless atmosphere, where the background parameters vary only in the vertical direction and neglecting wind shear terms, the acoustic wave equation for atmospheric infrasound propagation can be written as[34,35]

$$\frac{1}{c^2}\left(\frac{\partial}{\partial t} + \boldsymbol{v}_{0H} \cdot \nabla_H\right)^2 p - \nabla_H^2 p - \rho_0 \frac{\partial}{\partial z}\left(\frac{1}{\rho_0}\frac{\partial p}{\partial z}\right) = 0. \tag{3}$$

Here $\boldsymbol{v}_{0H} = \boldsymbol{v}_{0H}(z)$ is the horizontal wind component (vertical winds are negligible), ∇_H is the horizontal gradient operator, $\rho_0 = \rho_0(z)$ is the density, and $c = c(z)$ is the adiabatic speed of sound. Assuming an acoustic medium at rest, Eq. (3) reduces to the ordinary wave equation that is typically used for the modeling of ocean acoustics.

Numerous numerical methods provide different solutions to the acoustic and elastic linear wave equations. Solutions of the time-space and frequency-space forms of the wave equation are commonly obtained by using finite-difference,[36,37] spectral methods,[38] finite/spectral elements,[39] and ray methods.[40,41] Modeling wave propagation in layered media with smooth lateral variations, like the ocean, is usually done by using normal modes[42] and parabolic-equation[37] methods for solving the frequency-wavenumber (f-k) wave equation.

In order to use the solution for the coupled elastic-acoustic model as suggested by Schmidt and Tango,[43] for the coupled atmosphere system, the effective sound speed approximation is used. In this approximation, the horizontal wind in the direction of propagation is added to the sound speed. The resulting effective sound speed is then used to model atmospheric infrasound propagation. It has been shown (e.g., Assink *et al.*[35]) that this approximation is sufficient for many applications. Mathematically, the approximation corresponds to the following. In the frequency-(horizontal) wavenumber form of Eq. (3), the operator $(\partial/\partial t + \boldsymbol{v}_{0H} \cdot \nabla_H)/c$ can be written as $(i\omega - i\boldsymbol{k}_H \cdot \boldsymbol{v}_{0H})/c$. Approximating $\boldsymbol{k}_H \approx \omega \hat{k}_H / c$, where $\hat{k}_H$ is the horizontal direction of propagation, the operator can be approximated by

$$\begin{aligned}\frac{i\omega}{c}\left(1 - \frac{\boldsymbol{v}_{0H} \cdot \hat{k}_H}{c}\right) &= \frac{i\omega}{c}\left(\frac{1}{1 + \frac{\boldsymbol{v}_{0H} \cdot \hat{k}_H}{c}}\right) + \mathcal{O}(M^2) + \cdots \\ &\approx \frac{i\omega}{c + \boldsymbol{v}_{0H} \cdot \hat{k}_H} \equiv \frac{i\omega}{c_{\text{eff}}}.\end{aligned} \tag{4}$$

The effective sound speed, c_{eff}, overestimates the effects of the winds on the propagation. Therefore, this approximation holds for (1) small vertical propagation angles, (2) in-plane propagation, and (3) low Mach number, $\mathrm{M} = |\boldsymbol{v}_{0H}|/c$.[44,45]

Plugging Eq. (4) into the frequency domain form of Eq. (3) yields

$$k_{z,\text{eff}}^2 p + \rho_0 \frac{1}{\partial z}\left(\frac{1}{\rho_0}\frac{\partial p}{\partial z}\right) = 0. \tag{5}$$

The vertical wavenumber is defined as $k_{z,\text{eff}} = \sqrt{k_{\text{eff}}^2 - k_H^2}$ and $k_{\text{eff}} = \omega / c_{\text{eff}}$. In the case of a dissipative atmosphere, absorption is frequency-dependent, and the winds can cause a Doppler shift to the waves' frequencies. Nevertheless, this effect is small for infrasonic frequencies.[46]

Assink *et al.*[35] studied the influence of the effective speed of sound approximation on infrasound propagation in a lossless atmosphere with a maximum Mach number of $\mathrm{M} = 0.4$. It is shown that (1) overestimation of effect of horizontal wind on refraction leads to underestimates of travel-time and trace velocity and (2) overestimation of the acoustic frequency leads to small inaccuracies of the estimated absorption. However, for low wind conditions, the influence of this approximation is negligible. In both cases, the amplitudes were not affected by the effective speed of sound approximation.

The fast field program (FFP) solves the Helmholtz equation for a horizontally stratified medium. This method is based on dividing the medium (velocity and density profiles) into small homogeneous layers, while the layers are coupled to each other by explicitly imposing the boundary conditions between them. This allows one to take the influence of an exponentially decreasing density on the acoustic field into account. In addition, it allows one to easily handle discontinuities between solid-fluid, solid-gas, and fluid-gas interfaces as well as providing a direct control over the simulated frequencies and wavenumbers. Therefore, the contribution of the different coupling mechanisms is distinguishable and quantified. In seismology, this approach is known as the reflectivity method.[47]

Using M piecewise homogeneous layers with a thickness of 20 m each implies that within each layer, $m = 1 \cdots M$, the density is constant and the vertical operator in Eq. (5) takes the form of $\partial^2/\partial z^2$. Moreover, the relation between the particle displacement and pressure is $w_m = \nabla p_m / \rho_{m0} \omega^2$. Since the density is constant within each layer, the curl of the displacement, w_m, is zero. Therefore, the displacement field in the atmosphere can be expressed by an independent potential within each layer.

https://doi.org/10.1121/10.0000792

Following that, in seismo-acoustic modeling the displacement field in each layer can be expressed in terms of a scalar potential for the acoustic medium and a scalar and a vector potential for the elastic medium. These potentials are the basis of the Green's functions of the displacement field. In the case of a homogeneous elastic medium, the wavefield can be decoupled into P-SV and SH motions. These decoupled motions can be expressed by two scalar potentials and one scalar potential, respectively.[2] In this work, we assume the medium to be horizontally stratified, axisymmetric, with coupled elastic-acoustic layers. For such set-up, the SH motion has no contribution to the acoustic wavefield in the fluid layers, and it will be neglected.

Under these assumptions, the displacement field within a layer at a distance r and depth z, in the acoustic medium can be written in cylindrical coordinates as

$$u_m^f(r,z) = \frac{\partial \Phi_m^f}{\partial r},$$
$$w_m^f(r,z) = \frac{\partial \Phi_m^f}{\partial z}. \tag{6}$$

Accounting only for P-SV motion in the elastic medium, the displacement field within a layer can be written as

$$u_m^s(r,z) = \frac{\partial \Phi_m^s}{\partial r} + \frac{\partial^2 \Psi_m^s}{\partial r \partial z},$$
$$w_m^s(r,z) = \frac{\partial \Phi_m^s}{\partial z} - \frac{1}{r}\frac{\partial}{\partial r} r \frac{\partial \Psi_m^s}{\partial r}. \tag{7}$$

In Eq. (6), the potential Φ_m^f represent the compressional-wave potential, and in Eq. (7) the potentials Φ_m^s and Ψ_m^s represent the compressional-wave and shear-wave potentials, respectively. All potentials must satisfy the wave equation. u_m and w_m are the horizontal and vertical displacements, respectively, and suffixes f and s correspond to fluid and solid medium. Hooke's law, which relates stress and strain in an elastic medium, is used to compute the corresponding stress field.

Since the different coupling mechanisms are frequency and wavenumber dependent, solving the wave equation in the f-k domain is beneficial. Defining Λ as an arbitrary potential, the frequency-domain wave equation is known as the Helmholtz equation $[\nabla^2 + k_m^2]\Lambda_m(r,z) = 0$. Applying the Hankel transform to the Helmholtz equation yields the depth-separated Helmholtz equation

$$\left[\frac{d^2}{dz^2} + k_z^2\right]\Lambda_m(k_r,z) = 0, \tag{8}$$

where $k_z = \sqrt{k_m^2 - k_r^2}$ is the vertical wavenumber, k_r is the horizontal wavenumber, and k_m is the layer wavenumber. Depending on the medium type in each layer, the potential Λ and the vertical wavenumber k_z will be replaced according to the potentials and propagation velocities presented in Table I. For the elastic layers, solutions of both compressional-wave and shear-wave potentials need to be combined in order to obtain a complete representation of P-SV motion. Moreover, only a combination of both potentials gives rise to surface waves which are significant contributors to the seismo-acoustic wavefield.

TABLE I. Potential types, wavenumber definitions, and propagation velocities for the different media. The seismic wave velocities are functions of the density and Lamé parameters. The speed of sound in the ocean depends on the unperturbed pressure and density p_0 and ρ_0, the temperature T, and salinity S. The effective speed of sound in the atmosphere depends on the unperturbed pressure and density, temperature T, and the horizontal winds.

Wave type	Earth	Ocean	Atmosphere
Compressional	Φ^s	Φ^f	Φ^f
	$k = \omega/v_p$	$k = \omega/c_{\text{ocean}}$	$k = \omega/c_{\text{eff}}$
	$v_p(\rho_0, \lambda, \mu)$	$c_{\text{ocean}}(p_0, \rho_0, T, S)$	$c_{\text{eff}}(p_0, \rho_0, v_{0H})$
Shear	Ψ^s		
	$\tilde{k} = \omega/v_s$		
	$v_s(\rho_0, \mu)$		

Equation (8) is an ordinary differential equation in the vertical axis, and the solution for each layer is a linear combination of the homogeneous solution $\Lambda_m(k_r,z)$ and a particular solution $\hat{\Lambda}_m(k_r,z)$ if a source is present. Exact solutions for Eq. (8) can be written in terms of wavenumber integrals. The latter implies that field's exact Green's functions in the f-k domain can be retrieved. Decomposing the solution into up and down going wavefields allows for a straightforward implementation of the boundary conditions (BC) in the numerical solution. Defining A^- and A^+, respectively, as the up and down going wavefield amplitudes, the compressional-wave potential solution can be written as $\Phi_m(k_r,z) = A^- e^{-ik_z z} + A^+ e^{ik_z z}$. Its frequency domain representation is

$$\Phi_m(r,z) = \int_0^\infty [A^- e^{-ik_z z} + A^+ e^{ik_z z}] J_0(k_r r) k_r dk_r, \tag{9}$$

and $J_0(k_r r)$ is the Bessel function of the first kind. Similarly, $\Psi_m(r,z)$ is represented as

$$\Psi_m(r,z) = \int_0^\infty \frac{1}{k_r}\left[B^- e^{-i\tilde{k}_z z} + B^+ e^{i\tilde{k}_z z}\right] J_0(k_r r) k_r dk_r. \tag{10}$$

The $1/k_r$ factor ensures that the two potentials have the same dimensions due to an extra spatial derivative of the shear potential in Eq. (8). When $k_r > k_m$ or $k_r > \tilde{k}_m$, the vertical wavenumber of the potentials is imaginary. This part of the spectrum is known as evanescent, and its amplitude decays exponentially with vertical distance. As k_r increases with increasing frequency or decreasing trace velocity, k_z and $\tilde{k}_z$ obtain a larger imaginary value and consequently the wavefield component decays over a shorter distance. This property plays an essential role in the coupling process and affects the emitted infrasonic wave amplitude. This is further discussed in Secs. IV and V.

The potentials' coefficients are obtained using the direct global matrix (DGM) method, which is based on solving the continuity equations for all the interfaces (BC between the

layers) as well as the top and bottom BC simultaneously.[43] The BC for a solid-solid interface are the continuity of normal and tangential stress and vertical and horizontal displacements. A fluid-fluid interface requires the continuity of normal stress and vertical displacement. Finally, the BC at a solid-fluid interface are the continuity of vertical displacement and normal stress, and the vanishing of the tangential stress. Note that as the shear wavefield is part of both vertical displacement and normal stress, the SV motion contributes to the acoustic field in the fluid layer.

Discrete variations in the medium properties (density and velocity) are handled through the BC. These properties are encompassed in the equations of displacement and stress. The BC at the top and bottom layers can be free surface, rigid surface, or radiation condition. The presented solution allows for an exact implementation of the boundary conditions between the layers. This is in contrast to finite-difference discretization, which is often used in acoustic propagation models. Therefore, one can study the interaction of the wavefields in the different media in a straightforward manner and without any numerical approximations.

In this work, a compressional monopole source is used. The medium response for such a source, in terms of the compressional-wave potential, is

$$\hat{\Phi}(k_r, z) = \frac{S(\omega)}{4\pi} \int_0^\infty \frac{e^{ik_z|z-z_s|}}{ik_z} J_0(k_r r) k_r dk_r, \tag{11}$$

where z_s is the source depth and $S(\omega)$ is the frequency-domain source function. Depending on its position, the expressions for the wavefield components can be derived using Eqs. (6) and (7), and can be included in the continuity equations in the DGM. Source functions like an S-wave point source and a double-couple force will generate different wavefields and radiation patterns that will affect the radiated pressure field in the atmosphere. For simplicity, this study will use only the compressional monopole source.

The Green's function $\Lambda_m(r, z)$ is obtained after applying the inverse Hankel transform. As the inverse Hankel transform is computationally expensive, this transform is typically replaced in algorithms by the fast Fourier transform (FFT). This is an accurate approximation, except for near-field computations or steep propagation angles. Hence, the FFP algorithm gets its name from the use of the FFT algorithm to evaluate the horizontal wavenumber integral. Following Ref. 48, the discrete form of Eq. (9) is

$$\Lambda_m(r_j, z) = dk_r e^{(\epsilon + ik_{\min})r_j} \sqrt{\frac{1}{2\pi r_j}} e^{-i\pi/4} \times \sum_{l=0}^{L-1} \left[\Lambda_m(k_l, z) e^{ir_{\min} l dk_r} \sqrt{k_l} \right] e^{i(2\pi lj/L)}, \tag{12}$$

where L is the number of the discrete wavenumbers and ranges k_l and r_j, respectively. Their corresponding intervals are dk and dr. ϵ is a parameter with a small value on the order of dk which is added for numerical stability. A detailed explanation can be found in Chap. 4 of the text book by Jensen *et al.*[49]

Transforming the Green's functions from frequency-domain to the time-domain yields the wavefield's space-time representation. Considering a set of N frequencies and their corresponding frequency-space Green's functions, a broadband signal can be obtained using Fourier synthesis. That is to say, an inverse FFT (IFFT) is applied to the frequency-domain wavefield, convolved with the frequency-domain source function, $\Lambda_m(r, z, t) = \mathrm{IFFT}[\Lambda_m(r, z, \omega) \cdot S(\omega)]$.

IV. NUMERICAL EXAMPLES

A. Underwater source

Radiation of acoustic waves from an underwater source into the atmosphere involves the coupling of homogeneous and inhomogeneous body waves. Their contribution to long-range infrasound propagation in terms of transmission loss (TL) is investigated with a model that consists of a smooth atmospheric profile above a Munk oceanic profile (Fig. 1). The TL describes the decrease in the wave intensity, and it is defined as

$$\mathrm{TL} = 10 \log_{10} \left(\frac{p(r, z)^2 / \rho(z) c(z)}{p_s(r_0, z_s)^2 / \rho(z_s) c(z_s)} \right), \tag{13}$$

where $p_s(r_0, z_s)$ is the pressure produced by the source at a distance of $r_0 = 1$ m and at a depth z_s in unbounded medium. Also, the same definition holds for an underground source as long as a compressional monopole source is used. In case of other source types, the stresses are anisotropic, and a different scaling should be considered.[50]

A point source is placed at a depth of 1000 m, and its radiation into the atmosphere is simulated for two discrete frequencies. At 50 Hz, the source's distance from the ocean-atmosphere interface is larger than 30 wavelengths ($kz > 1$). The top frame in Fig. 1 shows the narrowband field from such a source. In the ocean, the propagation is bounded in two waveguides. With its axis at a depth of 1 km, the sound fixing and ranging channel (SOFAR) is the first waveguide. The second waveguide is the entire water column with its margins at the ocean-atmosphere interface and the ocean bottom. At this frequency, the ocean-atmosphere interface behaves almost as a perfect reflector, preventing most of the acoustic waves from radiating into the atmosphere; only a small fraction of the wavefield, with steep propagation angles, radiates above the source. Due to the exponential decay of the inhomogeneous waves and the high-frequency source, this part of the spectrum decays and vanishes before reaching the atmosphere.

Reducing the simulated frequency to 0.5 Hz, the distance to the ocean-atmosphere interface decreases to half a wavelength ($kz < 1$). For this setup, the interface becomes transparent to the evanescent regime, allowing waves with trace velocities of at least the sound speed at sea level (i.e., 340 m/s) to radiate into the atmosphere. These waves are then trapped in the tropospheric (first 10 km) and stratospheric (between

https://doi.org/10.1121/10.0000792

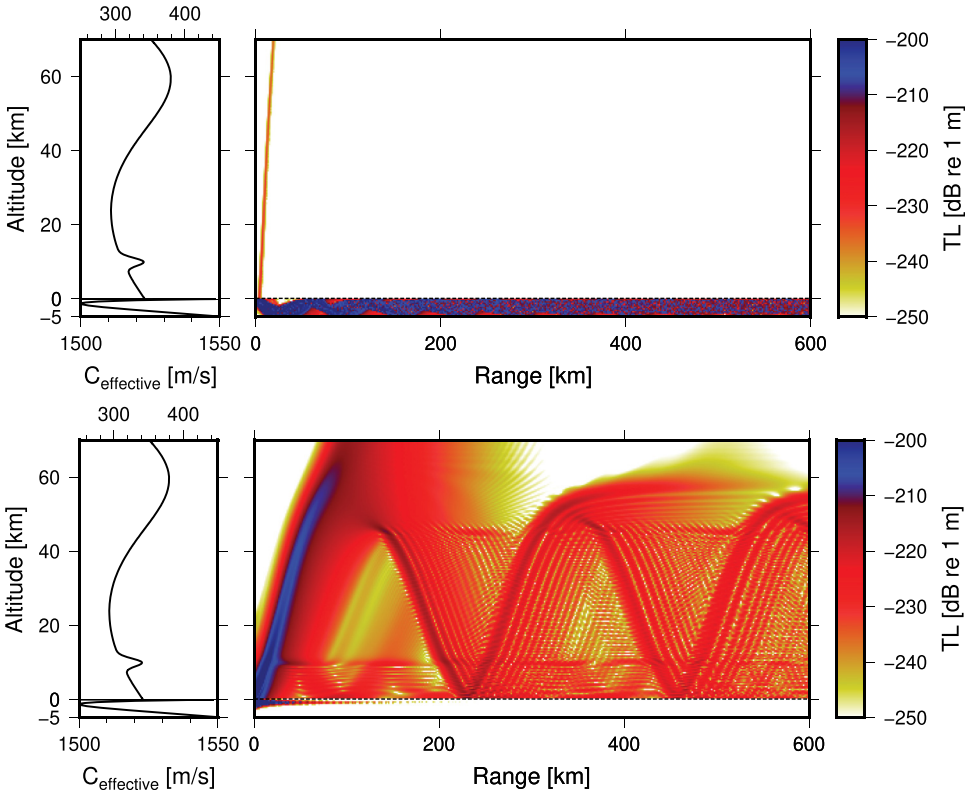

FIG. 1. (Color online) Propagation from an underwater source at a depth of 1000 m. The top frame shows propagation from a 50 Hz source. In the ocean, the waves are bounded by the entire water column as well as being trapped by the SOFAR channel. The radiated wave into the atmosphere corresponds to the direct acoustic wave from the source. Due to its high trace velocity, the wave propagates upwards. The bottom frame shows propagation from a 0.5 Hz source. Due to its low frequency, 1000 m equals a third of a wavelength. For these source parameters, the interface becomes transparent to the evanescent waves, allowing it to get trapped in both tropospheric (10 km) and stratospheric (60 km) waveguides.

Earth's surface and 50 km) waveguides and propagate over vast horizontal distances (Fig. 1, lower frame).

Before reaching the atmosphere, the inhomogeneous spectrum of the source undergoes an exponential decay that depends on the source depth and the vertical wavenumber which depends on the trace velocity. Subsequently, both transmitted amplitudes and radiation patterns differ for different source depths. Figure 2 shows the effect of the source depth on the transmitted acoustic pressure. An increase in the source depth leads to a decrease in the coupled wave amplitude, and therefore a decrease in TL [Fig. 2(a)].

Variations in the radiation patterns due to different source depth are evident when comparing the normalized modal amplitudes. As the source depth increases, the relative amplitudes of the lower trace velocities decrease while the amplitudes of the higher trace velocities increase. This is further detailed by the ratios of the normalized modes [Fig. 2(c)]. For this particular atmospheric model, the lower trace velocity modes correspond to tropospheric propagation, and the higher trace velocity modes correspond to stratospheric propagation. The exponential decay of the evanescent waves is inversely proportional to the trace velocity. Therefore, the low trace velocity evanescent waves decay faster, and emit waves with lower amplitudes into the atmosphere. Consequentially, higher amplitude waves are trapped in the stratospheric waveguide for deeper sources, when compared to the tropospheric waveguide.

B. Earth-atmosphere coupling from an underground source

In an Earth-atmosphere system with an underground compressional monopole source, infrasound waves radiate into the atmosphere due to the coupling of inhomogeneous body waves and surface waves. Broadband simulations are used to investigate the effect of the elastic properties and the source depth on the radiated infrasonic waves in the atmosphere. The model consists of either a soft or hard elastic halfspace (Table II) with the same smooth atmospheric profile from Fig. 1 on top of it. A source is placed at depths of 1000, 1500, and 2000 m, and a Ricker wavelet with a central frequency of 0.5 Hz is used as a source function.

Figure 3 shows the simulated pressure timeseries in the atmosphere (1 km above the interface) from a source at a depth of 1000 m in the hard elastic halfspace. The first visible arrival is the air-coupled surface wave that travels along the interface with a trace velocity of 1800 m/s. After the surface wave, there is a sequence of different atmospheric phases. The direct wave that radiates from the source is visible over the first 50 km. Then, the first guided tropospheric arrival appears between 50 to 150 km from the source. At 120 km the second tropospheric bounce arrives, and at 220 km the first stratospheric arrival appears. At further distances, the atmospheric arrivals consist of two tropospheric and two stratospheric phases. A zoom-in to such arrivals is shown in the boxed signal. It shows two tropospheric (I_w) and two stratospheric (I_s) signals. The small wiggle leading the first stratospheric arrival is a result of horizontal propagation across the Earth-atmosphere interface (diving wave or refracted wave). An f-k analysis reveals two main branches with trace velocities of 1800 and 330–400 m/s. These branches correspond to the surface wave and the inhomogeneous body waves, respectively (Fig. 3, right frame). A faint branch that corresponds to a trace velocity of

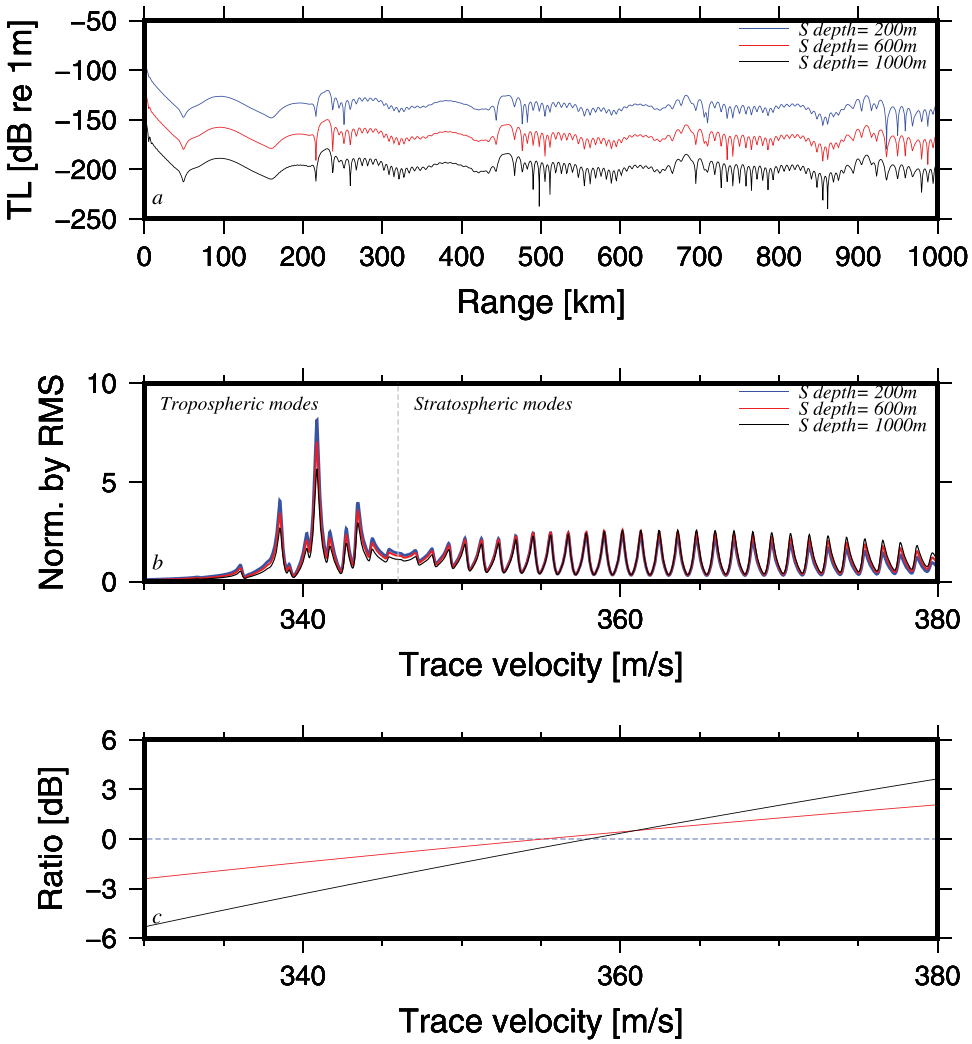

FIG. 2. (Color online) Simulated TL curves and propagating modes above ground for a 0.5 Hz source at different depths. (a) TL values decrease as the source depth increases. (b) The normalized modes show the effect of the source depth on the modal amplitudes. The exponential decay of the evanescent waves is wavenumber dependent. Therefore, waves with lower trace velocities decay faster. This behavior is evident in the increase of the stratospheric modes as the source depth enlarges. The dashed line at 345 m/s represents the transition between tropospheric to stratospheric modes. (c) Ratios of the normalized modal amplitudes (compared to the blue curve) imply that as the source depth increases, the relative stratospheric-phases amplitudes will be higher than the tropospheric ones.

5000 m/s represents the coupling from the homogeneous P wave. As predicted, the homogeneous P wave has the smallest contribution to the atmospheric perturbations due to the high density and velocity contrast.

Simulation for a source in a soft bottom show a better coupling to the atmosphere (Fig. 4). Beside having stronger amplitudes, the main difference is the lower surface wave velocity. Coupling from a slower elastic layer may result in air-coupled surface waves also getting trapped in the atmospheric waveguides. This mechanism may explain the observed secondary infrasound source in sedimentary basins.[17,20] Accounting for viscoelastic attenuation will change the relative coupled amplitudes from evanescent and surface waves. While the general trend is a reduction of the signals' amplitudes, surface waves will experience a faster decay than body waves. The effect on the coupled acoustic signal in the atmosphere is modeled for a sample scenario in the Appendix.

TABLE II. Rock properties used in the calculation of the coupled fields for a soft and hard bottom.

Elastic medium	ρ [kg/m^3]	V_p[m/s]	V_s[m/s]
Soft	1900	1500	600
Hard	2700	5000	2000

Following the analysis of the modes in Fig. 2, the effect of the source depth is demonstrated in Fig. 5. As the source depth increases, the relative amplitude of the second stratospheric phase, which corresponds to higher trace velocity, increases compared to the other atmospheric phases. The different acoustic partitioning in the atmosphere is a consequence of the exponential decay of the evanescent waves in the elastic layers.

With the new understandings of the Earth-atmosphere coupling mechanisms, let us re-examine the detected signals from the 12 February 2013 and 6 January 2016 North Korean underground nuclear tests. Assink *et al.*[51] (Fig. 4) detected three infrasound phases from the 2013 test and one phase from the January 2016 test. The three prominent phases are associated with tropospheric propagation (I_w), stratospheric propagation (I_s), and a combined propagation path (I_{ws}). On the other hand, in 2016, a weak signal was detected, and it was not possible to determine the nature of its propagation. It was postulated that a combination of unfavorable propagation condition and a deeper source

https://doi.org/10.1121/10.0000792

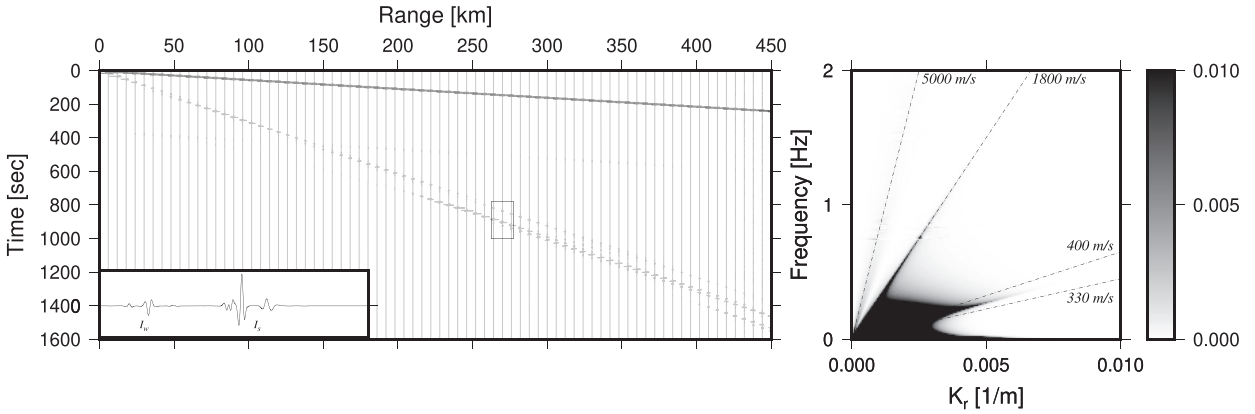

FIG. 3. Synthetic pressure timeseries. Broadband simulation for a source at a depth of one kilometer with a central frequency of 0.5 Hz in the hard bottom. The first arrivals correspond to the air-coupled surface wave with a trace velocity of 1800 m/s. Following it are the first tropospheric refractions in the range of 50–150 km, and second tropospheric refractions between 120 and 250 km. The first stratospheric refraction appears at approximately 220 km after the tropospheric phases. A zoom-in on the boxed signal reveals a signal that consists of two tropospheric (I_w) and two stratospheric (I_s) phases. Right: f-k plot shows the dispersion relation of the propagating waves in the atmosphere. Coupling from the direct P wave from the source is barely not visible (branch of 5000 m/s). The 1800 m/s branch represents the air-coupled surface wave, and the 300–400 m/s cone shows the amplitudes of the coupled evanescent waves.

during the 2016 test are the reasons for the weak signal. While further exploring the conclusions of that study, the influence of the source depth can now be deduced in more detail. Considering a deeper source and the exponential decay of the evanescent waves, the amplitude of the coupled signal in 2016 was one order of magnitude weaker than in 2013. Such decay levels the signal's amplitude with the background noise. Moreover, the radiation pattern from deeper sources makes it more likely that the observed signal was a stratospheric phase.

V. SUMMARY AND DISCUSSION

Observations of long-range infrasound signals originated from underwater and underground sources contradict the usually considered free surface behavior of the ocean-atmosphere and Earth-atmosphere interfaces, which implies almost total reflection. While wave propagation in solids, fluids, and solid-fluid systems has been well studied, long-range infrasound propagation from subsurface sources is not yet well understood. In this work, coupling mechanisms are proposed and studied regarding long-range infrasound propagation. The presented results are essential for the understanding of the complex infrasound signals originating from seismo-acoustic events.

The FFP is used to model the seismo-acoustic coupling between the solid Earth, the ocean, and the atmosphere under the variation of source depth and frequency, and properties of the subsurface and atmospheric conditions. Modeling in the f-k domain provides a convenient way to distinguish between the different coupling mechanisms and study their contribution to the acoustic wavefield in the atmosphere. Results show the important role of evanescent coupling between the Earth, ocean, and the atmosphere and the ability of the emitted waves to get trapped in the atmospheric waveguides and propagate over vast distances. Evanescent waves with low trace velocities decay faster than ones with high trace velocities. The differences in the decay rate lead to an inhomogeneous radiation pattern in the atmosphere, which leads to different acoustic partitioning in the atmospheric waveguides. Therefore, for the same

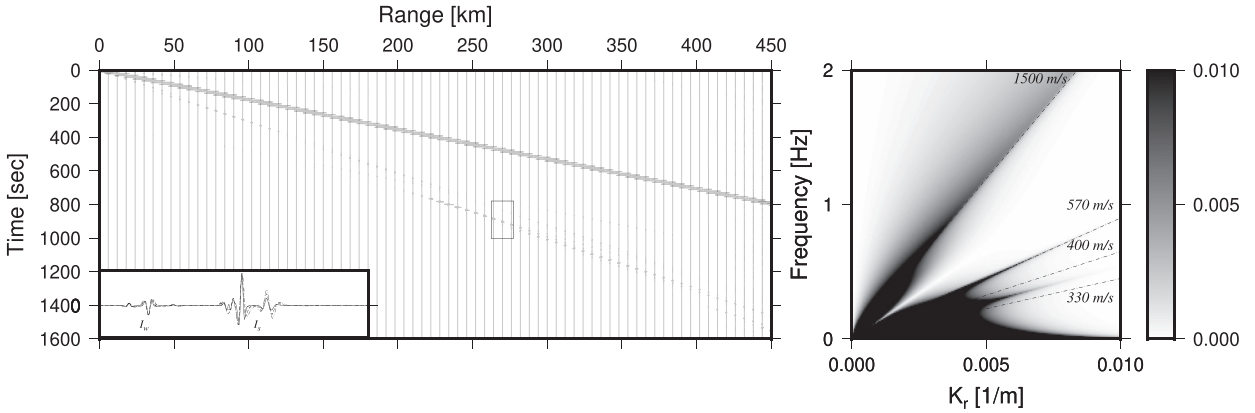

FIG. 4. Synthetic pressure timeseries. Broadband simulation for a source at a depth of one kilometer with a central frequency of 0.5 Hz in the soft bottom. The direct P wave (branch of 1500 m/s) is prominent for frequencies up to 2 Hz. Higher amplitudes of the surface wave (570 m/s branch) and the coupled inhomogeneous waves are also apparent.

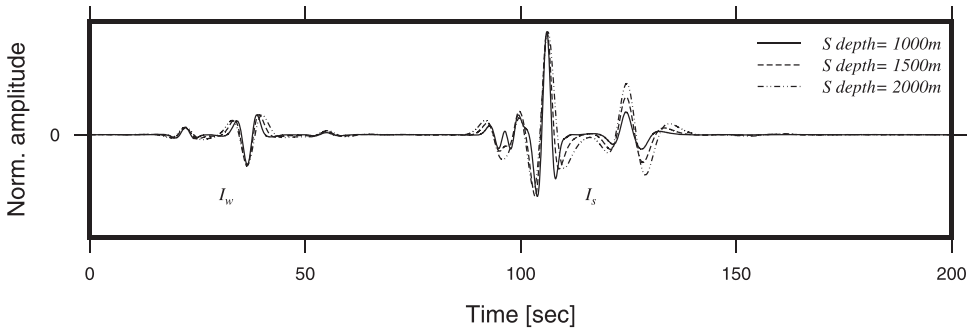

FIG. 5. Comparison of the normalized signals arriving at 270 km (boxed signal Fig. 4) for different source depths. It shows that as the source depth increases, the relative amplitude of the second stratospheric phase increases compares to the other phases. Such behavior agrees with the modal analysis in Fig. 2 and the theoretical predictions of Godin (Ref. 21).

atmosphere and different source depths, the relative amplitudes of the atmospheric phases will change. Particularly, as the source depth increases, the relative amplitudes of the higher trace velocity phases are larger than the lower trace velocity phases.

In the Earth-atmosphere system, surface waves have a significant contribution to the acoustic radiation into the atmosphere. Nevertheless, the radiated waves do not necessarily get trapped and propagate in the atmospheric waveguides. The propagation direction of the coupled surface waves in the atmosphere depends on the atmospheric sound speed relative to the surface wave velocity. Therefore, only surface waves with trace velocities in the order of the atmospheric sound speed profile will enable the radiated waves to get trapped in the atmospheric waveguides.

The presented study assumes a horizontally layered medium to reduce complexity and understand the underlying mechanisms of seismo-acoustic coupling. Although it provides essential insights into the effect of the coupling mechanisms on long-range infrasound propagation, it cannot accurately simulate events in a range dependent medium and with topographic features. Nevertheless, some conclusions on different setups can be derived. For example, the presence of a region with a low seismic velocity can lead to the contribution of surface waves to long-range infrasound propagation.

The inhomogeneous radiation from underwater and underground sources brings up the question, how much information about the subsurface or underwater source can be retrieved. The effect of a different source depth on the atmospheric wavefield has been shown. However, the inverse problem regarding the source intensity, depth, and mechanism remains a challenge. Moreover, the interaction with complex topography and range dependent profile, and the influence of absorption will be the subject of future research.

ACKNOWLEDGMENTS

G.A. is funded through the Marie Curie Action WAVES from the European Union within H2020, Grant No. 641943. The contribution of L.G.E. is funded through a VIDI project from the Netherlands Organization for Scientific Research (NWO), Project 864.14.005. We would like to thank Pieter Smets and Shahar Shani-Kadmiel for fruitful discussions, and the anonymous reviewers for their constructive comments.

APPENDIX: THE EFFECT OF VISCOELASTIC ATTENUATION

The effect of viscoelastic attenuation is tested by introducing complex Lamé parameters and complex medium wavenumbers. Their imaginary part is derived from empirical Q factor relations.[52,53] Based on the seismic velocities of the soft layer in Table II, quality factors of $Q_p = 78$ and $Q_s = 39$ are calculated for pressure and shear waves, respectively. A narrowband simulation is carried out accounting for attenuation. Its effect is demonstrated in Fig. 6. The "ringing" in the blue curve (no attenuation) is the signature of the radiated surface wave. Despite its large amplitude, small features that correspond to the tropospheric and stratospheric propagation are still visible. Attenuation has two main effects on the coupled waves: (1) rapid decay of the surface wave leads to no observable signal from it and (2) the radiated acoustic waves are attributed to coupling from inhomogeneous body waves.

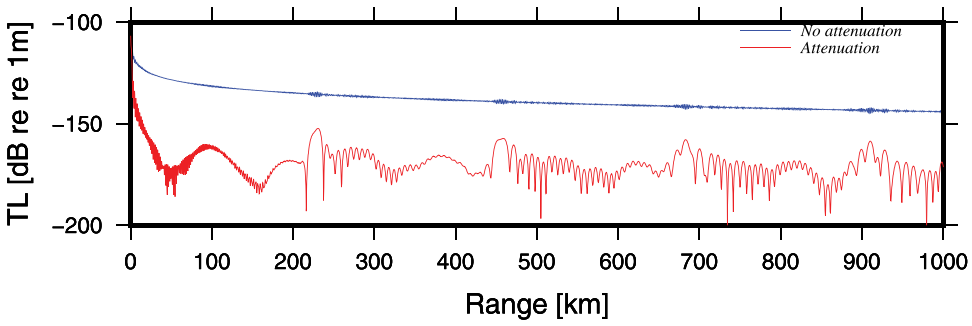

FIG. 6. (Color online) Results show that the radiated acoustic waves are attributed to coupling from inhomogeneous body waves while the contribution from surface waves is negligible. Moreover, depending on the source depth, a decrease of 15–25 dB in TL is obtained.

[1]P. Campus and D. R. Christie, "Worldwide observations of infrasonic waves," in *Infrasound Monitoring for Atmospheric Studies* (Springer Netherlands, Dordrecht, 2009), pp. 185–234.
[2]K. Aki and P. G. Richards, *Quantitative Seismology* (University Science Books, Mill Valley, CA, 2002), p. 700.
[3]H. Benioff, M. Ewing, and F. Press, "Sound waves in the atmosphere generated by a small earthquake," Proc. Natl. Acad. Sci. USA **37**(9), 600–603 (1951).
[4]B. A. Bolt, "Seismic air waves from the Great 1964 Alaskan earthquake," Nature **202**(4937), 1095–1096 (1964).
[5]W. L. Donn and E. S. Posmentier, "Ground-coupled air waves from the Great Alaskan Earthquake," J. Geophys. Res. **69**(24), 5357–5361, https://doi.org/10.1029/JZ069i024p05357 (1964).
[6]T. Mikumo, "Atmospheric pressure waves and tectonic deformation associated with the Alaskan earthquake of March 28, 1964," J. Geophys. Res. **73**(6), 2009–2025, https://doi.org/10.1029/JB073i006p02009 (1968).
[7]J. M. Young and G. E. Greene, "Anomalous infrasound generated by the Alaskan earthquake of 28 March 1964," J. Acoust. Soc. Am. **71**(2), 334–339 (1982).
[8]A. Ben-Menahem and M. Vered, "Modeling of atmospheric nuclear explosions over a mountainous region by vertical and horizontal single forces," Bull. Seismol. Soc. Am. **65**(4), 971–980 (1975).
[9]H. Kanamori, J. Mori, D. L. Anderson, and T. H. Heaton, "Seismic excitation by the space shuttle Columbia," Nature **349**(6312), 781–782 (1991).
[10]B. Tauzin, E. Debayle, C. Quantin, and N. Coltice, "Seismoacoustic coupling induced by the breakup of the 15 February 2013 Chelyabinsk meteor," Geophys. Res. Lett. **40**(14), 3522–3526, https://doi.org/10.1002/grl.50683 (2013).
[11]J. P. Mutschlecner and R. W. Whitaker, "Infrasound from earthquakes," J. Geophys. Res. **110**(D1), D01108, https://doi.org/10.1029/2004JD005067 (2005).
[12]S. Watada, T. Kunugi, K. Hirata, H. Sugioka, K. Nishida, S. Sekiguchi, J. Oikawa, Y. Tsuji, and H. Kanamori, "Atmospheric pressure change associated with the 2003 Tokachi-Oki earthquake," Geophys. Res. Lett. **33**(24), L24306, https://doi.org/10.1029/2006GL027967 (2006).
[13]T. Mikumo, T. Shibutani, A. Le Pichon, M. Garces, D. Fee, T. Tsuyuki, S. Watada, and W. Morii, "Low-frequency acoustic-gravity waves from coseismic vertical deformation associated with the 2004 Sumatra-Andaman earthquake (Mw = 9.2)," J. Geophys. Res.: Solid Earth **113**(12), B12402, https://doi.org/10.1029/2008JB005710 (2008).
[14]D. N. Green, J. Guilbert, A. Le Pichon, O. Sebe, and D. Bowers, "Modelling ground-to-air coupling for the shallow ML 4.3 Folkestone, United Kingdom, earthquake of 28 April 2007," Bull. Seismol. Soc. Am. **99**(4), 2541–2551 (2009).
[15]A. Le Pichon, P. Mialle, J. Guilbert, and J. Vergoz, "Multistation infrasonic observations of the Chilean earthquake of 2005 June 13," Geophys. J. Int. **167**(2), 838–844 (2006).
[16]E. Marchetti, G. Lacanna, A. Le Pichon, D. Piccinini, and M. Ripepe, "Evidence of large infrasonic radiation induced by earthquake interaction with alluvial sediments," Seismol. Res. Lett. **87**(3), 678–684 (2016).
[17]S. Shani-Kadmiel, J. D. Assink, P. S. M. Smets, and L. G. Evers, "Seismoacoustic coupled signals from earthquakes in central Italy: Epicentral and secondary sources of infrasound," Geophys. Res. Lett. **45**(1), 427–435, https://doi.org/10.1002/2017GL076125 (2018).
[18]J. Artru, T. Farges, and P. Lognonné, "Acoustic waves generated from seismic surface waves: Propagation properties determined from Doppler sounding observations and normal-mode modelling," Geophys. J. Int. **158**(3), 1067–1077 (2004).
[19]L. G. Evers, D. Brown, K. D. Heaney, J. D. Assink, P. S. Smets, and M. Snellen, "Evanescent wave coupling in a geophysical system: Airborne acoustic signals from the Mw 8.1 Macquarie Ridge earthquake," Geophys. Res. Lett. **41**(5), 1644–1650, https://doi.org/10.1002/2013GL058801 (2014).
[20]J. Assink, G. Averbuch, S. Shani-Kadmiel, P. Smets, and L. Evers, "A seismo-acoustic analysis of the 2017 North Korean nuclear test," Seismol. Res. Lett. **89**(6), 2025–2033 (2018).
[21]O. A. Godin, "Anomalous transparency of water-air interface for low-frequency sound," Phys. Rev. Lett. **97**(16), 164301 (2006).
[22]B. E. McDonald and D. C. Calvo, "Enhanced sound transmission from water to air at low frequencies," J. Acoust. Soc. Am. **122**(6), 3159–3161 (2007).
[23]O. A. Godin, "Sound transmission through water–air interfaces: New insights into an old problem," Contemp. Phys. **49**(2), 105–123 (2008).
[24]L. Rayleigh, "On waves propagated along the plane surface of an elastic solid," Proc. London Math. Soc. **s1-17**(1), 4–11 (1885).
[25]T. J. I. Bromwich, "On the influence of gravity on elastic waves, and, in particular on the vibrations of an elastic globe," Proc. London Math. Soc. **s1-30**(1), 98–165 (1898).
[26]R. Stoneley, "The effect of the ocean on Rayleigh waves," Geophys. J. Int. **1**(s7), 349–356 (1926).
[27]M. A. Biot, "The interaction of Rayleigh and Stoneley waves in the ocean bottom*," Bull. Seismol. Soc. Am. **42**(1), 81–93 (1952).
[28]J. G. Scholte, "The range of existence of Rayleigh and Stoneley waves," Geophys. J. Int. **5**(s5), 120–126 (1947).
[29]N. G. Brower, D. E. Himberger, and W. G. Mayer, "Restrictions on the existence of leaky Rayleigh waves," IEEE Trans. Sonics Ultrason. **26**(4), 306–308 (1979).
[30]W. M. Ewing, W. S. Jardetzky, F. Press, and A. Beiser, "Elastic waves in layered media," Phys. Today **10**(12), 27–28 (1957).
[31]A. Ben-Menahem and S. J. Singh, *Seismic Waves and Sources* (Springer, New York, 1981), p. 1108.
[32]O. A. Godin, "Low-frequency sound transmission through a gas-solid interface," J. Acoust. Soc. Am. **129**(2), EL45–EL51 (2011).
[33]J. Achenbach, *Wave Propagation in Elastic Solids* (Elsevier, New York, 1984).
[34]L. M. Brekhovskikh and O. A. Godin, *Acoustics of Layered Media II: Point Sources and Bounded Beams* (Springer, Berlin, 1999), p. 524.
[35]J. Assink, R. Waxler, and D. Velea, "A wide-angle high Mach number modal expansion for infrasound propagation," J. Acoust. Soc. Am. **141**(3), 1781–1792 (2017).
[36]K. R. Kelly and R. W. Ward, "Synthetic seismograms: A finite-difference approach," **41**(1), 2–161 (1976).
[37]F. D. Tappert, "The parabolic approximation method," in *Wave Propagation and Underwater Acoustics* (Springer, Berlin, 1977), pp. 224–287.
[38]D. Kosloff, D. Kessler, A. Q. Filho, E. Tessmer, A. Behle, and R. Strahilevitz, "Solution of the equations of dynamic elasticity by a Chebychev spectral method," Geophysics **55**(6), 734–748 (1990).
[39]D. Komatitsch and J. Tromp, "Introduction to the spectral element method for three-dimensional seismic wave propagation," Geophys. J. Int. **139**(3), 806–822 (1999).
[40]J. Virieux, "P-SV wave propagation in heterogeneous media: Velocity-stress finite-difference method," Geophysics **51**(4), 889–901 (1986).
[41]V. Cerveny, *Seismic Ray Theory* (Cambridge University Press, Cambridge, 2001), p. 724.
[42]C. L. Pekeris, "The propagation of a pulse in the atmosphere," Proc. R. Soc. A: Math. Phys. Eng. Sci. **171**(947), 434–449 (1939).
[43]H. Schmidt and G. Tango, "Efficient global matrix approach to the computation of synthetic seismograms," Geophys. J. R. Astron. Soc. **84**(2), 331–359 (1986).
[44]O. A. Godin, "An effective quiescent medium for sound propagating through an inhomogeneous, moving fluid," J. Acoust. Soc. Am. **112**(4), 1269–1275 (2002).
[45]R. Waxler, "Modal expansions for sound propagation in the nocturnal boundary layer," J. Acoust. Soc. Am. **115**(4), 1437–1448 (2004).
[46]R. Waxler, J. Assink, and D. Velea, "Modal expansions for infrasound propagation and their implications for ground-to-ground propagation," J. Acoust. Soc. Am. **141**(2), 1290–1307 (2017).
[47]K. Fuchs and G. Müller, "Computation of synthetic seismograms with the reflectivity method and comparison with observations," Geophys. J. Int. **23**(4), 417–433 (1971).
[48]F. R. DiNapoli and R. L. Deavenport, "Theoretical and numerical Green's function field solution in a plane multilayered medium," J. Acoust. Soc. Am. **67**(1), 92–105 (1980).
[49]F. B. Jensen, W. A. Kuperman, M. B. Porter, and H. Schmidt, *Computational Ocean Acoustics* (Springer, New York, 2011).

[50]S. D. Frank, R. I. Odom, and J. M. Collis, "Elastic parabolic equation solutions for underwater acoustic problems using seismic sources," J. Acoust. Soc. Am. **133**(3), 1358–1367 (2013).
[51]J. D. Assink, G. Averbuch, P. S. M. Smets, and L. G. Evers, "On the infrasound detected from the 2013 and 2016 DPRK's underground nuclear tests," Geophys. Res. Lett. **43**(7), 3526–3533, https://doi.org/10.1002/2016GL068497 (2016).
[52]T. M. Brocher, "Key elements of regional seismic velocity models for long period ground motion simulations," J. Seismol. **12**(2), 217–221 (2008).
[53]S. Shani-Kadmiel, M. Tsesarsky, J. N. Louie, and Z. Gvirtzman, "Geometrical focusing as a mechanism for significant amplification of ground motion in sedimentary basins: Analytical and numerical study," Bull. Earthquake Eng. **12**(2), 607–625 (2014).